nature communications

Article

https://doi.org/10.1038/s41467-025-57736-3

Broadband microwave-rate dark pulse microcombs in dissipation-engineered $LiNbO_3$ microresonators

Received: 23 April 2024

Accepted: 3 March 2025

Published online: 10 March 2025

Check for updates

Xiaomin Lv[1,2,6], Binbin Nie[1,6], Chen Yang[1,6] ✉, Rui Ma[3], Ze Wang[1], Yanwu Liu[1], Xing Jin[1], Kaixuan Zhu[1], Zhenyu Chen[3], Du Qian[1], Guanyu Zhang[1], Guowei Lv[1], Qihuang Gong[1,2,4,5], Fang Bo[3] ✉ & Qi-Fan Yang[1,2,4,5] ✉

Kerr microcombs generated in optical microresonators provide broadband light sources bridging optical and microwave signals. Their translation to thin-film lithium niobate unlocks second-order nonlinear optical interfaces such as electro-optic modulation and frequency doubling for completing comb functionalities. However, the strong Raman response of $LiNbO_3$ has complicated the formation of Kerr microcombs. Until now, dark pulse microcombs, requiring a double balance between Kerr nonlinearity and normal group velocity dispersion as well as gain and loss, have remained elusive in $LiNbO_3$ microresonators. Here, by incorporating dissipation engineering, we demonstrate dark pulse microcombs with 25 GHz repetition frequency and 200 nm span in a high-Q $LiNbO_3$ microresonator. Resonances near the Raman-active wavelengths are strongly damped by controlling phase-matching conditions of a specially designed pulley coupler. The coherence and tunability of the dark pulse microcombs are also investigated. Our work provides a solution to realize high-power microcombs operating at microwave rates on $LiNbO_3$ chips, promising new opportunities for the monolithic integration of applications spanning communication to microwave photonics.

Optical frequency combs, consisting of discrete spectral lines aligned to equidistant frequency grids, serve as a coherent link between optical and microwave signals[1]. They have become the cornerstone for precision spectroscopy[2] and metrology[3], and their potential to enhance a diverse range of applications hinges on instrumental advancements that prioritize reduced size, weight, and power consumption. This aspiration has been realized in optical microresonators as microcombs, which harness resonantly-enhanced nonlinear optical processes for comb generation[4]. To date, mode-locked microcombs have been demonstrated in many microresonator platforms, such as MgF_2[5], silica[6], Si_3N_4[7], SiC[8], and $LiNbO_3$[9].

$LiNbO_3$ has become an appealing comb-generating material due to its various optical nonlinearities, broad transparency window, and compatibility with integrated photonics[10]. The most well-known Pockels and Kerr effects have enabled electro-optic combs[11–13] and soliton microcombs[9,14–18] in $LiNbO_3$ microresonators. Furthermore, their combination is expected to complete microcomb functionalities. Since electro-optically modulated soliton microcombs[19] and highly-

---

[1]State Key Laboratory for Artificial Microstructure and Mesoscopic Physics and Frontiers Science Center for Nano-optoelectronics, School of Physics, Peking University, Beijing 100871, China. [2]Hefei National Laboratory, Hefei, China. [3]Nankai University, Tianjin, China. [4]Collaborative Innovation Center of Extreme Optics, Shanxi University, Taiyuan, China. [5]Peking University Yangtze Delta Institute of Optoelectronics, Nantong, China. [6]These authors contributed equally: Xiaomin Lv, Binbin Nie, Chen Yang. ✉e-mail: ycoptics@pku.edu.cn; bofang@nankai.edu.cn; leonardoyoung@pku.edu.cn

efficient frequency doublers[20] are accessible on Z-cut $LiNbO_3$ microresonators, self-referenced microcombs are underway for compact spectrometers[21–25], miniaturized optical clocks[26,27], low-noise microwave generation[28–30], and high-precision ranging[31–33].

The inclusion of Raman nonlinearity in comb-forming processes has introduced a range of novel phenomena. In materials with broadband Raman gain, such as silica, stimulated Raman scattering (SRS) can result in a redshift of the comb spectra[34] or provide co-propagating, pulsed Raman gain for the formation of a secondary soliton microcomb[35]. In contrast, $LiNbO_3$, a Raman-active crystal with several narrow-band vibrational energy levels (Fig. S7 in supplementary information (SI)), is inclined to produce continuous-wave Raman gain from individual comb lines. This results in continuous-wave Raman lasing in microresonators, thereby complicating the comb formation process[15,36,37].

Mitigating SRS in $LiNbO_3$ microresonators is essential for soliton microcomb generation[18,19]. The challenge is amplified for another important class of Kerr microcombs known as dark pulse microcombs. Unlike the sech^2-shaped soliton microcombs, dark pulse microcombs appear as flat-top pulses in the microresonator[38–43], exhibiting superior pump-to-comb conversion efficiency and high comb line power. Although these features are appealing for communications[44–46] and microwave photonics[47], the high-power comb lines near the spectral center of dark pulse microcombs also promotes continuous-wave SRS (Section I in SI), especially in microresonators with small free spectral ranges (FSRs) where optical modes more easily resonate with Stokes photons[36,48]. Consequently, dark pulse microcombs remain challenging to realize in $LiNbO_3$ microresonators.

In this article, we present a dissipation engineering approach to mitigate SRS in an integrated high-Q $LiNbO_3$ microresonator, where pulley waveguide couplers are designed to introduce wavelength-dependent losses to the microresonator. Consequently, we demonstrate the generation of dark pulse microcombs with repetition frequencies as low as 24.8 GHz and spectra spanning over 200 nm. Furthermore, we show the tuning of repetition frequency over 292 kHz by adjusting the laser-cavity detuning and characterize the phase noise performance, highlighting their potential for various applications at optical and microwave frequencies.

Results

Dissipation engineering

SRS and Kerr-induced four-wave mixing are both third-order nonlinear optical processes, with the threshold power for their initiation following similar scaling laws based on the dissipation rates of the microresonator (κ). For Raman lasing to occur, the pump energy inside the microresonator must exceed

$$E_{\mathrm{th,R}} = \frac{\kappa_R}{2g_R}, \tag{1}$$

where g_R is the Raman gain coefficient and κ_R is the dissipation rate of the mode involved in Raman lasing. In the case of Kerr nonlinearity, and ignoring dispersion requirements, the pump energy required to initiate degenerate four-wave mixing is given by

$$E_{\mathrm{th,K}} = \frac{\sqrt{\kappa_{\mathrm{S}}\kappa_{\mathrm{AS}}}}{2g_K}, \tag{2}$$

where κ_{S} and κ_{AS} represent the dissipation rates for the Stokes and anti-Stokes modes, respectively. In $LiNbO_3$, the Kerr nonlinear coefficient g_K is often significantly smaller than the Raman gain coefficient g_R. To raise the Raman lasing threshold to a level that does not interfere with Kerr microcomb formation, the dissipation rate of the Raman lasing mode should be substantially larger than that of the Stokes and anti-Stokes modes near the pump mode. This is the target of dissipation engineering in this work.

The optical dissipation in microresonators comprises both intrinsic and external components. The former (κ_o) is primarily influenced by material absorption and surface scattering, which is challenging to engineer in the frequency domain. On the other hand, external dissipation (κ_{ext}) is dictated by waveguide coupling, which can be tuned in the frequency domain by designing phase-matching conditions between the waveguide and microresonator. Therefore, controlling κ_{ext} provides a route for dissipation engineering.

We first consider the most widely-used coupler design, i.e., straight waveguide couplers, whose coupling to a ring resonator results in a confined coupling region due to limited spatial overlap. As the wave propagates along the waveguide, the effective distance between the waveguide and microring rapidly increases, leading to phase mismatching and a gradual increase in κ_{ext} with wavelength due to modal leakage (Fig. 1a). We simulate comb formation in a normal-dispersion $LiNbO_3$ microresonator with a straight waveguide coupler based on the generalized Lugiato-Lefever equation augmented by SRS (see "methods"). The FSR of the microresonator is set significantly smaller than the Raman gain bandwidth. The nearly constant dissipation profile gives rise to Raman lasing when the microresonator is pumped by a continuous-wave laser (Fig. 1b). Additionally, four-wave mixing interactions between the pump and Raman laser initiate modulational instability (MI), resulting in chaotic waveforms within the microresonator. Numerical simulations using a broader selection of pumping parameters (pump power and laser-cavity detuning) reveal the phase diagram, which excludes dark pulse microcombs (Fig. 1c).

This situation can be overturned by employing pulley waveguide couplers, which wrap around the resonator with a consistent gap, thereby considerably enhancing the coupling length compared to traditional straight waveguide coupling (Fig. 1d). By carefully designing the geometry of the waveguide and the microring, it is possible to achieve phase-matching conditions at specific wavelengths. Consequently, κ_{ext} experiences a rapid increase towards the phase-matching wavelength. When modes within the Raman gain bandwidth experience much larger dissipation rates than modes near the pump, dark pulse microcombs can form in the microresonator, with a typical optical spectrum shown in Fig. 1e. Despite the presence of Raman lasing and modulational instability at high pump power levels, a distinct region indicating the existence of dark pulse microcombs emerges in the phase diagram (Fig. 1f), highlighting the efficacy of dissipation engineering.

Device characterization

We fabricate dissipation-engineered microring resonators on 570-nm-thick Z-cut lithium niobate on insulator wafers (Fig. 2a). The geometry of the microresonator, characterized by a radius of 817 μm, an etching depth of 300 nm, and a top width of 2.2 μm, is chosen to induce normal group velocity dispersion (GVD). Experimentally, we measure the resonant frequencies of the fundamental transverse-electric (TE) mode family over a wavelength range of 1460 nm to 1630 nm using tunable continuous-wave lasers calibrated by a Mach-Zehnder interferometer. The measured integrated dispersion, defined as $D_{\mathrm{int}} = \omega_\mu - \omega_0 - D_1\mu = \sum_{n\geq 2} D_n\mu^n/n!$, where μ is mode index relative to the pump mode, ω_μ represents the resonant frequency of the μ_{th} mode, and $D_1/2\pi$ is the free spectral range (FSR), is plotted in Fig. 2b. The FSR of the microresonator is found to be 24.803 GHz. Polynomial fitting of the integrated dispersion data reveals the second-order dispersion $D_2/2\pi$ = −6.2 kHz. Nevertheless, the experimentally measured mode family dispersion exhibits local deviations from the simulated results at several wavelengths. These discrepancies are likely attributed to interactions with other transverse modes in the multimode waveguides.

The pulley coupler, characterized by a bus waveguide width of 1.756 μm, a pulley angle of 15 degrees, and a constant gap of 450 nm (Fig. S6 in SI), is anticipated to exhibit increased coupling losses at wavelengths exceeding 1600 nm. These wavelengths feature strong

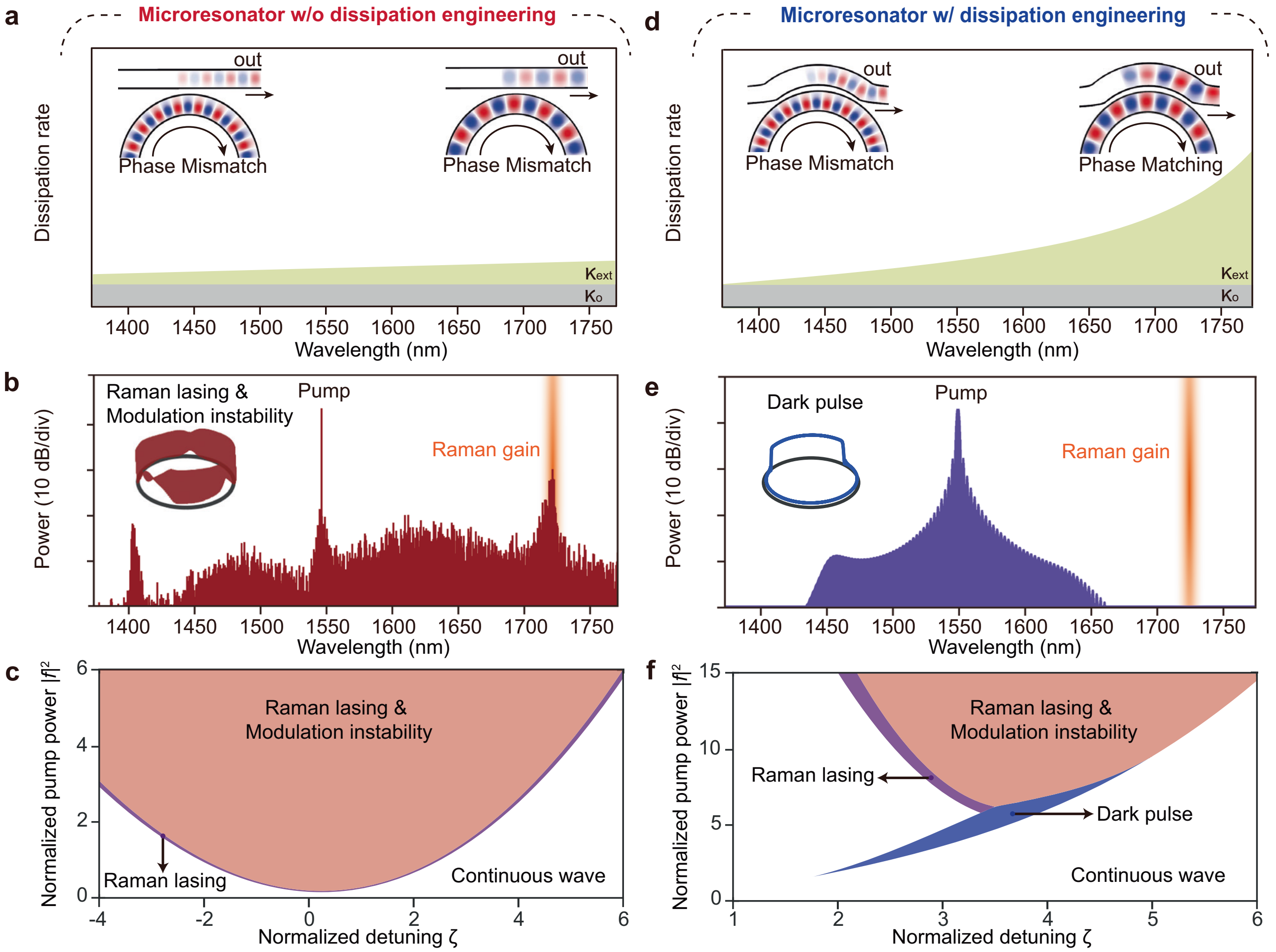

Fig. 1 | Dissipation engineering for dark pulse microcomb generation. **a** Dissipation rate versus wavelength for microrings coupled to straight bus waveguides. κ_o: intrinsic loss; κ_{ext}: external coupling loss. **b** Simulated optical spectrum and temporal profile of microcomb in microresonators without dissipation engineering. The color gradient indicates the Raman gain. **c** Simulated phase diagram as a function of pump power and laser-cavity detuning in microresonators without dissipation engineering. The normalization of detuning and pump power is defined in Methods, and the details of simulating the phase diagrams are provided in the supplementary information. **d** Dissipation rate versus wavelength for microrings coupled to pulley bus waveguides. **e** Simulated optical spectrum and temporal profile of microcomb in microresonators with dissipation engineering. **f** Simulated phase diagram as a function of pump power and laser-cavity detuning in microresonators with dissipation engineering. The blue area indicates the maximum existence range of dark pulses generated from an initial seed, which are determined by verifying their stability in the generalized Lugiato-Lefever equation.

Raman gain for 1563.2 nm pump lasers, as depicted in Fig. 2c and Fig. S7 (see SI). To investigate the impact of the pulley waveguide, we analyze the broadband transmission spectrum of the microresonator. Given that the intrinsic loss remains relatively stable within this spectral range, we utilized this knowledge ($Q_o \approx 4$ ~ 5 M) to distinguish between intrinsic and external coupling losses by applying Lorentzian fitting to the transmission spectra. Our analysis reveals that the microresonator transitions from over-coupling to under-coupling and then returns to over-coupling as the wavelength increases from 1460 nm to 1630 nm. Notably, the total dissipation rates reach $2\pi \times 350$ MHz at 1600 nm, representing a threefold increase compared to those observed near 1563.2 nm. This increase is expected to result in a corresponding threefold rise in the Raman lasing threshold. The excellent agreement between our measured and simulated results underscores the precision with which the device geometry is controlled during fabrication.

Generation of dark pulse microcombs

An amplified continuous-wave laser pumps the microresonator at around 1563.2 nm for comb generation. The laser is scanned from the red-detuned side towards the blue-detuned side of the mode. The transmission spectra of the pump and other comb lines are selected using a tunable fiber Bragg-grating filter (Fig. 3a). Low-noise steps appear first on the transmission spectra, corresponding to mode-locked microcombs. Further increasing the laser frequency results in chaotic transmission spectra, referred to as MI. As shown in Fig. 3b, the optical spectra of MI manifest two Raman lasers with frequency shifts of 153 cm^{-1}, and 628 cm^{-1}, respectively, corresponding to the optical phonon modes of $E(TO)_1$ and $A(TO)_4$ (Fig. S7 in SI)[49,50]. Other sidebands arise from the four-wave mixing processes and are not coherent with each other.

The photorefractive effect in LiNbO$_3$ allows for bi-directional accessing the low-noise steps in terms of tuning the laser frequency[9]. Each step corresponds to a different state of the dark pulse microcomb, and several representative optical spectra are displayed in Fig. 3c. The combs span from 1440 nm to 1640 nm, and Raman lasing actions are not observed. The spacings of the microcombs can be adjusted from single FSR to 4 FSR. Microcombs with multiple-FSR spacing exhibit enhanced power per comb line and an extended spectral span captured by the optical spectral analyzer[51]. A few spikes are present on the spectra due to the coupling between the fundamental TE mode and other transverse modes[52]. These avoided mode crossings, along with SRS, indeed facilitate the initiation of

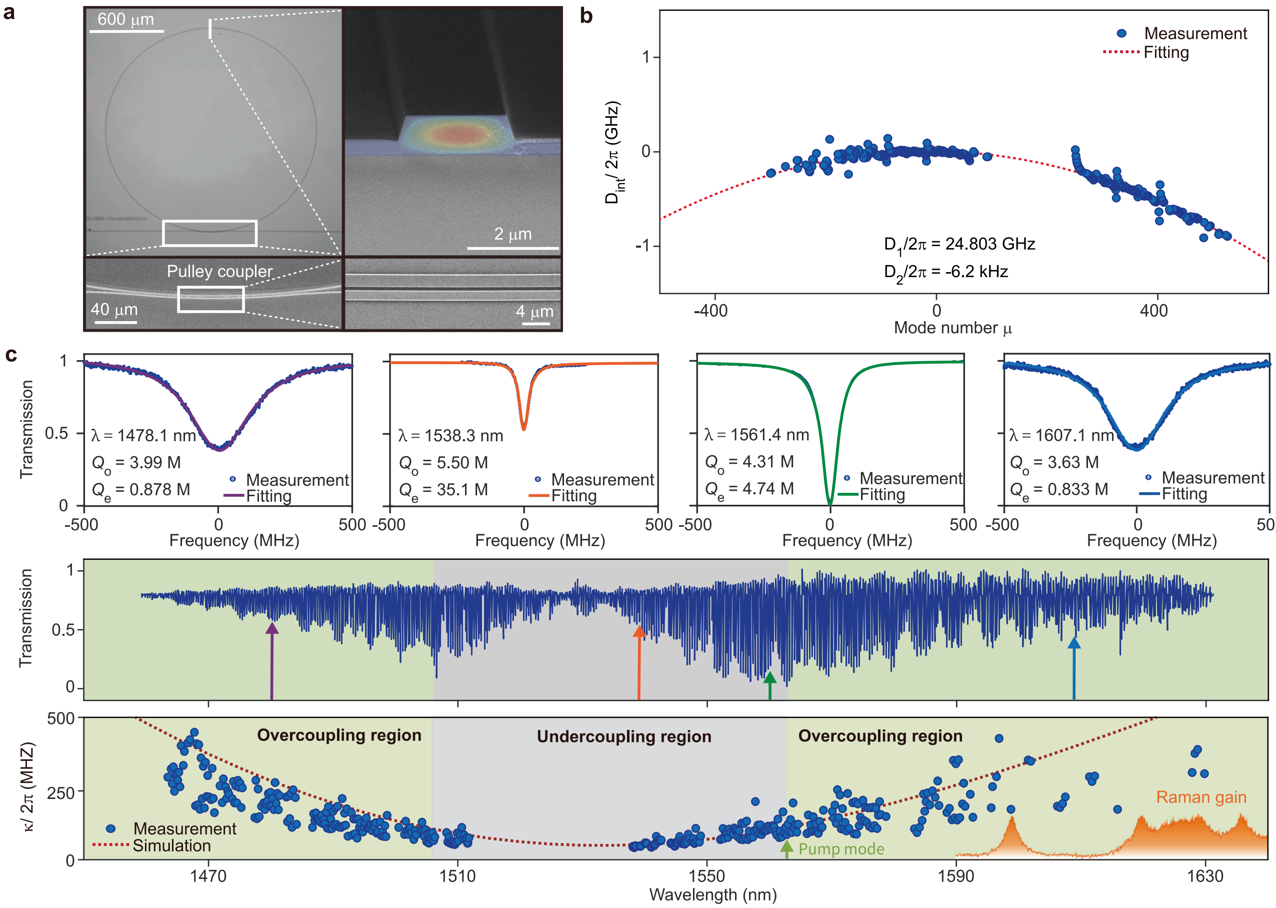

Fig. 2 | Device design and characterization. a Optical microscope images of $LiNbO_3$ microring (left, top) and scanning electron microscope images detailing various components: waveguide-coupled region (left, bottom), the cross-section of the microring waveguide (right, top), and a zoom-in view of the pulley waveguide coupler (right, bottom). The intensity profile of the fundamental TE mode is overlaid on the cross-section. **b** Integrated dispersion (D_{int}) of the fundamental TE mode family. The values of D_1 and D_2 are also listed. **c** Top panel: normalized transmission spectra of four typical resonances at different wavelengths. Middle panel: broadband transmission spectrum. The fringes caused by the reflection at the bus waveguide facets are removed using Fourier filtering. Bottom panel: measured and simulated total dissipation rates as a function of wavelength. Color shadings represent different coupling conditions. The pump mode and the corresponding Raman gain are also indicated.

parametric oscillations, and dark pulses can be generated at other pump wavelengths from 1552 nm to 1564 nm[38,53] (Fig. S8 in SI). With 260 mW pump power on the bus waveguide, the conversion efficiency of the pump to the comb line can be up to 4% by calibrating the losses in the measurement setup (Fig. S9 in SI). Photodetection of the single-FSR microcomb reveals a monotone electrical beatnote at 24.8038 GHz, corresponding to the repetition frequency of the microcomb. It unambiguously demonstrates the mode-locking of the microcomb.

We fine-tune the microcomb with single-FSR spacing by adjusting the laser-cavity detuning. The spectra acquired at two different detunings exhibit characteristic modulations with different periods determined by the duration of the dark pulse[38,54] (Fig. 3d). To infer the temporal profiles of the two states, we perform numerical simulations based on experimentally measured device parameters. The fittings of the optical spectra reveal flat-top pulses in the microresonator, with duration varied from 5.4 ps to 2.4 ps depending on the detuning. The relatively small duty cycle is a consequence of the near-zero dispersion of the microresonator. The deviation between the simulated intracavity spectra and the experimental results is attributed to the wavelength-dependent coupling to the bus waveguide. For instance, the dips observed in the experimental spectra near 1528 nm aligned with the under-coupled regime shown in Fig. 2c.

Microwave synthesis

We further investigate the tunability and noise performance of the microwave signal synthesized from the electrical beatnote (repetition frequency) of the dark pulse. The experimental setup is illustrated in Fig. 4a. In addition to the comb generation system, we actively monitor the comb power to stabilize the relative detuning between the pump laser and the resonance. As a result, we observe significant suppression of spectral drift over several hours, as demonstrated by the stability of the total power of the comb lines (Fig. 4b). This feedback control mechanism not only stabilizes the system but also allows precise tuning of the detuning, enabling access to different comb states, each characterized by distinct repetition frequencies. By adjusting the locking point, we achieve a tunability of the repetition frequency over a range of 292 kHz (Fig. 4c).

The phase noise of the repetition frequency is measured using a phase noise analyzer (Rohde & Schwarz FSWP50), while the phase noise of the pump laser is characterized using a delayed self-heterodyne interferometer (see "Methods"). A comparison of the laser phase noise and beatnote phase noise reveals similar spectral features at low offset frequencies (Fig. 4d), suggesting the presence of noise transduction between the two. This transduction likely arises from a combination of stimulated Raman scattering[52], higher-order dispersion[7], and avoided mode crossings[55], which introduce spectral shifts dependent on the laser-cavity detuning. As a result, the laser phase noise couples to the

https://doi.org/10.1038/s41467-025-57736-3

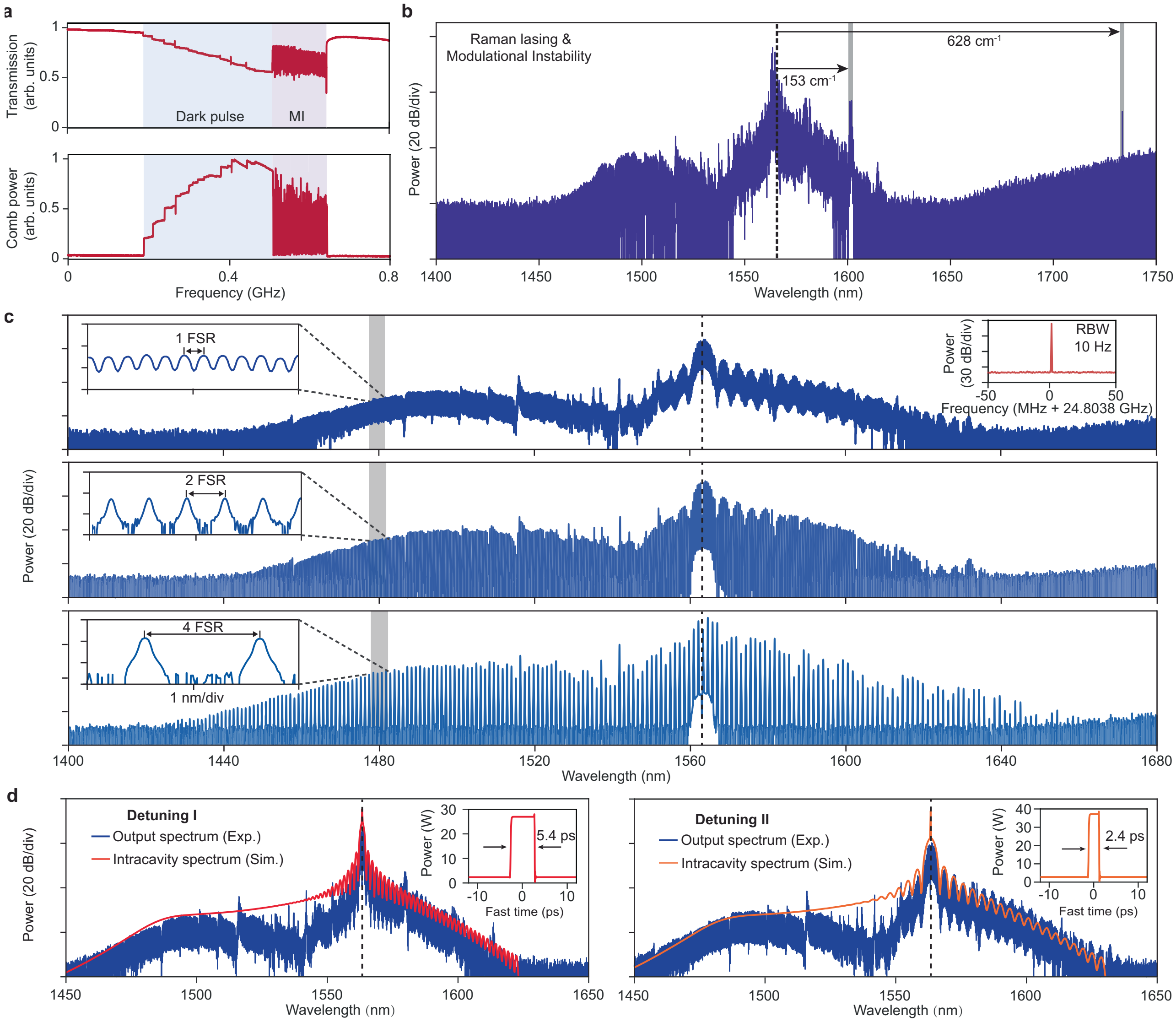

Fig. 3 | Formation of dark pulse microcombs. **a** Normalized transmitted pump power (top panel) and comb power (bottom panel) as a function of the increased pump laser frequency. **b** Optical spectrum of microcomb at MI state. Two Raman lasing modes are labeled with corresponding Raman shifts of 153 cm^{-1} and 628 cm^{-1}. **c** Optical spectra of dark pulse microcombs with different comb line spacing. The left insets show the zoom-in views of the comb lines. The right inset shows the measured electrical beatnote of the 1-FSR microcomb with 10-Hz resolution bandwidth (RBW). **d** Optical spectra of dark pulse microcombs for two different laser-cavity detunings. The simulated spectral envelopes of the microcombs are also plotted. The detunings are inferred from the simulations as 364 MHz and 400 MHz for left and right panels, respectively. Insets: simulated intracavity waveforms.

repetition frequencies. Furthermore, we find that the extent of this transduction varies with different detuning values. The lowest phase noise of the beatnote reaches -101 dBc/Hz at a 10 kHz offset and decreases to -143 dBc/Hz at a 1 MHz offset.

To quantify the transduction factor more precisely, we apply phase modulations to the pump laser, generating artificial spurs in the phase noise spectra. Given that the thermo-optic effect[56], pyroelectric-electro-optic effect[57], and photorefraction[9] can contribute to the discrepancy between the detuning noise and the pump noise, the phase modulation is set to 100 kHz to exceed the bandwidths of these effects. By comparing the spur levels at 100 kHz (inset of Fig. 4d), we estimate that the transduction factor can reach as high as −43 dB. Additionally, we observe another spur at 117 kHz, which is identified as originating from the relative intensity noise (RIN) of the pump laser. By matching the peak levels, we determine that the contribution of the pump RIN to the microwave phase noise is not the dominant limiting factor (see “Methods”).

Discussion

The demonstration of dark pulse microcombs in $LiNbO_3$ microresonators offers several advantages. First, realizing anomalous GVD at visible wavelengths is challenging for $LiNbO_3$, but dark pulse microcombs are compatible with the entire transparency window of $LiNbO_3$. This flexibility could drive the development of compact optical clocks[3], astronomical spectrometers[24,25], and other interdisciplinary applications[58]. Additionally, integrating dark pulse microcombs into $LiNbO_3$-based transmitters could leverage the high-power comb lines, offering excellent signal-to-noise ratios for massively parallel data transmission[44–46].

Future work is poised to equip Kerr microcombs with Pockels effect[9,17,19,59]. In this regard, the next step is to apply dissipation engineering to X-cut $LiNbO_3$ microresonators for comb generation. Despite the much stronger Raman response of TE-polarized extraordinary light in this platform, unlocking mode-locked Kerr microcombs in X-cut $LiNbO_3$ allows for integration with highly efficient

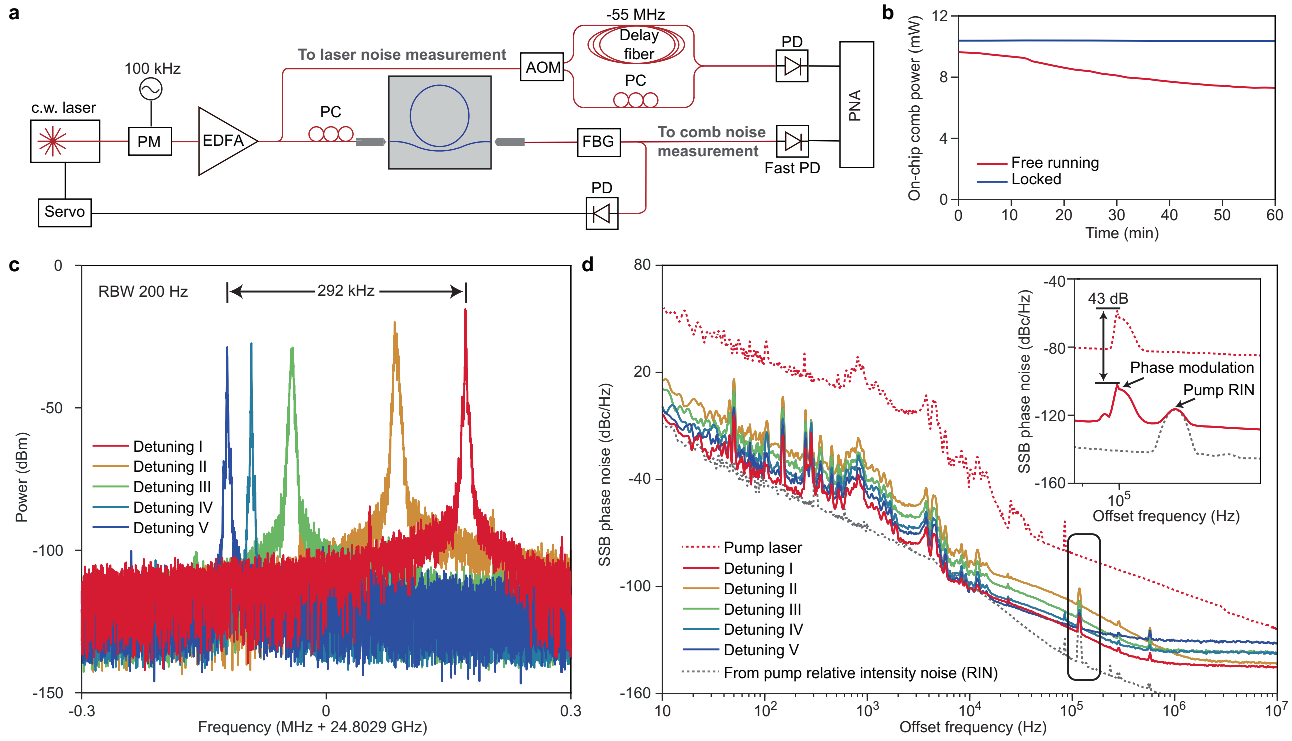

Fig. 4 | Microwave synthesis using dark pulse microcombs. a Experimental setup. PM: phase modulator; EDFA: erbium-doped fiber amplifier; PC: polarization controller; FBG: fiber Bragg grating; PD: photodetector; AOM: acousto-optic modulator; PNA: phase noise analyzer. **b** Evolution of comb power versus time. **c** Electrical beatnotes of dark pulse microcombs for 5 different laser-cavity detunings. **d** Single-sideband (SSB) phase noise of the repetition rates of the dark pulse microcombs and the pump laser. The contribution of the pump RIN to the phase noise is plotted as the gray dashed line. Inset: zoom-in view of the noise spectra near 100 kHz offset frequencies. The spurs induced by phase modulation and pump RIN are indicated.

electro-optic modulators[60] and frequency doublers[61] through planar fabrication processes in foundries. It should also open avenues for exploring the interplay between Kerr and Pockels effects in the comb-forming regime[62,63].

Methods

Device fabrication

Devices are fabricated from a commercial Z-cut $\mathrm{LiNbO_3}$-on-insulator wafer (NANOLN) with a 570-nm-thick $\mathrm{LiNbO_3}$ layer on top of a 4.7-μm-thick silica buffer layer. Electron-beam lithography is used to define the patterns of bus waveguides and microrings in ma-N 2405 resist with a thickness of 750 nm. The resist pattern is transferred to the $\mathrm{LiNbO_3}$ film using $\mathrm{Ar^+}$ plasma with an etching depth of 300 nm. The etching process yields a characteristic 60° angle of the sidewalls. The photoresist is removed by organic reagent and oxygen plasma. Finally, the redeposition on the surface of the sample is removed using SC1 solution.

Numerical simulations

The generalized Lugiato-Lefever equation (g-LLE), augmented with SRS and wavelength-dependent losses, provides a framework for simulating the evolution of intracavity optical fields[5,64–66]. This equation is expressed as

$$\begin{aligned}\frac{\partial A(\phi,t)}{\partial t} = &-i\delta\omega A-\mathcal{F}^{-1}\left\{\frac{\kappa(\mu)}{2}\tilde{A}_\mu\right\}+\sqrt{\frac{\kappa_{\mathrm{ext}}(0)P_{\mathrm{in}}}{\hbar\omega_0}}\\ &+i\frac{D_2}{2}\frac{\partial^2 A}{\partial\phi^2}+i(1-f_R)g_K|A|^2A\\ &+ig_K\frac{f_R A}{D_1}\int h_R\left(\frac{\phi-\phi'}{D_1}\right)|A(\phi')|^2d\phi'.\end{aligned}\qquad(3)$$

The slowly-varying field envelope $A(\phi,\ t)$ is normalized to photon number and studied in the rotation frame which rotates around the microresonator at the rate D_1. $\tilde{A}_\mu$ is the optical field of the μ_{th} mode, which is defined as $A(\phi,t)=\sum_\mu\tilde{A}_\mu e^{i\mu\phi}$. $\delta\omega$ is the frequency detuning of the pump laser relative to the mode. The pump power is denoted by P_{in}. The Kerr nonlinear coefficient is defined as $g_K=\hbar\omega_0^2n_2D_1/2\pi n_oA_{\mathrm{eff}}$, where n_o and n_2 are the linear and nonlinear refractive indices, respectively. A_{eff} is the nonlinear effective mode area. The total optical dissipation of the μ_{th} mode, $\kappa(\mu)=\kappa_o(\mu)+\kappa_{\mathrm{ext}}(\mu)$, accounts for both intrinsic ($\kappa_o(\mu)$) and external coupling ($\kappa_{\mathrm{ext}}(\mu)$) losses. The wavelength-dependent loss term is implemented in the frequency domain for convenience, with $\mathcal{F}^{-1}\{\cdot\}$ representing the inverse Fourier transform. In Fig. 1, the normalized detuning is defined as $\zeta=2\delta\omega/\kappa(0)$ and the normalized pump power is defined as $|f|^2=8g_K\kappa_{\mathrm{ext}}(0)P_{\mathrm{in}}/\kappa^3(0)\hbar\omega_0$.

$\mathrm{LiNbO_3}$ has several vibrational modes as shown in Fig. S7 (see SI). For simplicity but without loss of generality, in the simulation, we only include the mode with the strongest Raman response, *A(TO)*$_4$. The fractional contribution of Raman response to the total nonlinear polarization is denoted by f_R. The Raman response is formulated as a convolution product of the Raman response function and the temporal intracavity optical intensity. A standard form of the Raman response function for a single vibrational mode, $h_R(t)$, is given by[64,66]

$$h_R(t)=\begin{cases}\frac{\tau_1^2+\tau_2^2}{\tau_1\tau_2^2}\exp\left(-\frac{t}{\tau_2}\right)\sin\left(\frac{t}{\tau_1}\right) & ,t>0\\ 0 & ,t\le 0\end{cases},\qquad(4)$$

where τ_1 and τ_2 are the time constants characterizing the Raman response. Note that the Raman response function is only defined for $t>0$ for the reason of causality.

Numerical simulation of the g-LLE is performed using the split-step Fourier method, which involves 4096 modes. The parameters used to simulate the intracavity waveforms in Fig. 3d are: $D_1/2\pi$ = 24.8 GHz, $D_2/2\pi$ = −6.2 kHz, n_o = 2.0, n_2 = 1.8×10^{-19} m²/W, $A_{\rm eff}$ = 1.135 μm², $\omega_0/2\pi$ = 191.9 THz, $\kappa(\mu)/2\pi$ = $(-1.3\times10^{-9}\mu^4+1.0227\times10^{-6}\mu^3+2.5846\times10^{-3}\mu^2-0.49141\mu+70.747)$ MHz, f_R = 0.19, τ_1 = 8.3 fs, τ_2 = 544 fs[49,50,67,68]. The detuning I is set $\delta\omega_1/2\pi = 364$ MHz and the detuning II is set $\delta\omega_2/2\pi = 400$ MHz.

Laser noise measurement

The phase noise of the pump laser is measured using a delayed self-heterodyne setup. In this configuration, the laser beam is split into two paths: one path is frequency-shifted by 55 MHz via an acousto-optic modulator, while the other is delayed through a 1-km-long optical fiber. The recombined light is photodetected, and the resulting beat-note is analyzed with a phase noise analyzer to extract its single-sideband phase noise, $S_B(f)$. The laser's phase noise, $S_\phi(f)$, is then derived using the following equation[54]:

$$S_\phi(f) = S_B(f)\frac{1}{4\sin^2(\pi f\tau_d)}. \tag{5}$$

Here, τ_d represents the time delay between the two arms of the interferometer, which is 4.8821 μs in this work. To prevent divergence at offset frequencies where $\sin(\pi f\tau_d)=0$, a cut-off frequency is introduced as $1/\tau_d$. Beyond this threshold, only data points corresponding to offset frequencies of $(N+1/2)/\tau_d$, where N is a positive integer, are plotted to ensure the accurate representation of the phase noise data.

The RIN of the pump laser is measured using a non-amplified photodetector (Thorlabs DET01CFC/M) in conjunction with a phase noise analyzer operating in baseband measurement mode. The contribution of the laser's RIN, $S_I(f)$, to the microwave phase noise is quantified by the expression $\alpha S_I(f)/f^2$, where α represents the noise transduction factor.

Data availability

The data that support the plots within this paper and other findings of this study are available at https://doi.org/10.6084/m9.figshare.28282229[69].

Code availability

The codes that support the findings of this study are available at https://doi.org/10.6084/m9.figshare.28282229[69].

References

1. Diddams, S. A., Vahala, K. & Udem, T. Optical frequency combs: coherently uniting the electromagnetic spectrum. *Science* **369**, eaay3676 (2020).
2. Picqué, N. & Hänsch, T. W. Frequency comb spectroscopy. *Nat. Photon.* **13**, 146–157 (2019).
3. Ludlow, A. D., Boyd, M. M., Ye, J., Peik, E. & Schmidt, P. O. Optical atomic clocks. *Rev. Mod. Phys.* **87**, 637 (2015).
4. Kippenberg, T. J., Holzwarth, R. & Diddams, S. A. Microresonator-based optical frequency combs. *Science* **332**, 555–559 (2011).
5. Herr, T. et al. Temporal solitons in optical microresonators. *Nat. Photon.* **8**, 145–152 (2014).
6. Yi, X., Yang, Q.-F., Yang, K. Y., Suh, M.-G. & Vahala, K. Soliton frequency comb at microwave rates in a high-Q silica microresonator. *Optica* **2**, 1078–1085 (2015).
7. Brasch, V. et al. Photonic chip–based optical frequency comb using soliton Cherenkov radiation. *Science* **351**, 357–360 (2016).
8. Guidry, M. A., Lukin, D. M., Yang, K. Y., Trivedi, R. & Vučković, J. Quantum optics of soliton microcombs. *Nat. Photon.* **16**, 52–58 (2022).
9. He, Y. et al. Self-starting bi-chromatic $LiNbO_3$ soliton microcomb. *Optica* **6**, 1138–1144 (2019).
10. Boes, A. et al. Lithium niobate photonics: unlocking the electromagnetic spectrum. *Science* **379**, eabj4396 (2023).
11. Zhang, M. et al. Broadband electro-optic frequency comb generation in a lithium niobate microring resonator. *Nature* **568**, 373–377 (2019).
12. Rueda, A., Sedlmeir, F., Kumari, M., Leuchs, G. & Schwefel, H. G. Resonant electro-optic frequency comb. *Nature* **568**, 378–381 (2019).
13. Yu, M. et al. Integrated femtosecond pulse generator on thin-film lithium niobate. *Nature* **612**, 252–258 (2022).
14. Gong, Z. et al. Soliton microcomb generation at 2 μm in z-cut lithium niobate microring resonators. *Opt. Lett.* **44**, 3182–3185 (2019).
15. Gong, Z. et al. Photonic dissipation control for Kerr soliton generation in strongly Raman-active media. *Phys. Rev. Lett.* **125**, 183901 (2020).
16. Gong, Z., Liu, X., Xu, Y. & Tang, H. X. Near-octave lithium niobate soliton microcomb. *Optica* **7**, 1275–1278 (2020).
17. Lu, J. et al. Two-colour dissipative solitons and breathers in microresonator second-harmonic generation. *Nat. Commun.* **14**, 2798 (2023).
18. Song, Y., Hu, Y., Zhu, X., Yang, K. & Lončar, M. Octave-spanning Kerr soliton frequency combs in dispersion-and dissipation-engineered lithium niobate microresonators. *Light Sci. Appl.* **13**, 225 (2024).
19. He, Y. et al. High-speed tunable microwave-rate soliton microcomb. *Nat. Commun.* **14**, 3467 (2023).
20. Lu, J. et al. Periodically poled thin-film lithium niobate microring resonators with a second-harmonic generation efficiency of 250,000%/W. *Optica* **6**, 1455–1460 (2019).
21. Suh, M.-G., Yang, Q.-F., Yang, K. Y., Yi, X. & Vahala, K. J. Microresonator soliton dual-comb spectroscopy. *Science* **354**, 600–603 (2016).
22. Dutt, A. et al. On-chip dual-comb source for spectroscopy. *Sci. Adv.* **4**, e1701858 (2018).
23. Yang, Q.-F. et al. Vernier spectrometer using counterpropagating soliton microcombs. *Science* **363**, 965–968 (2019).
24. Obrzud, E. et al. A microphotonic astrocomb. *Nat. Photon.* **13**, 31 (2019).
25. Suh, M.-G. et al. Searching for exoplanets using a microresonator astrocomb. *Nat. Photon.* **13**, 25–30 (2019).
26. Papp, S. B. et al. Microresonator frequency comb optical clock. *Optica* **1**, 10–14 (2014).
27. Newman, Z. L. et al. Architecture for the photonic integration of an optical atomic clock. *Optica* **6**, 680–685 (2019).
28. Kudelin, I. et al. Photonic chip-based low-noise microwave oscillator. *Nature* **627**, 534–539 (2024).
29. Sun, S. et al. Integrated optical frequency division for microwave and mmWave generation. *Nature* **627**, 540–545 (2024).
30. Jin, X. et al. Microresonator-referenced soliton microcombs with zeptosecond-level timing noise. *arXiv Preprint* https://doi.org/10.48550/arXiv.2401.12760 (2024).
31. Suh, M.-G. & Vahala, K. J. Soliton microcomb range measurement. *Science* **359**, 884–887 (2018).
32. Trocha, P. et al. Ultrafast optical ranging using microresonator soliton frequency combs. *Science* **359**, 887–891 (2018).
33. Riemensberger, J. et al. Massively parallel coherent laser ranging using a soliton microcomb. *Nature* **581**, 164–170 (2020).
34. Yi, X., Yang, Q.-F., Yang, K. Y. & Vahala, K. Theory and measurement of the soliton self-frequency shift and efficiency in optical microcavities. *Opt. Lett.* **41**, 3419–3422 (2016).
35. Yang, Q.-F., Yi, X., Yang, K. Y. & Vahala, K. Stokes solitons in optical microcavities. *Nat. Phys.* **13**, 53–57 (2017).
36. Okawachi, Y. et al. Competition between Raman and Kerr effects in microresonator comb generation. *Opt. Lett.* **42**, 2786–2789 (2017).

37. Yu, M. et al. Raman lasing and soliton mode-locking in lithium niobate microresonators. *Light.: Sci. Appl.* **9**, 9 (2020).
38. Xue, X. et al. Mode-locked dark pulse Kerr combs in normal-dispersion microresonators. *Nat. Photon.* **9**, 594–600 (2015).
39. Lobanov, V., Lihachev, G., Kippenberg, T. & Gorodetsky, M. Frequency combs and platicons in optical microresonators with normal GVD. *Opt. Express* **23**, 7713–7721 (2015).
40. Kim, B. Y. et al. Turn-key, high-efficiency Kerr comb source. *Opt. Lett.* **44**, 4475–4478 (2019).
41. Helgason, Ó. B. et al. Dissipative solitons in photonic molecules. *Nat. Photon.* **15**, 305–310 (2021).
42. Jin, W. et al. Hertz-linewidth semiconductor lasers using CMOS-ready ultra-high-Q microresonators. *Nat. Photon.* **15**, 346–353 (2021).
43. Lihachev, G. et al. Platicon microcomb generation using laser self-injection locking. *Nat. Commun.* **13**, 1771 (2022).
44. Fulop, A. et al. High-order coherent communications using mode-locked dark-pulse Kerr combs from microresonators. *Nat. Commun.* **9**, 1598 (2018).
45. Jørgensen, A. et al. Petabit-per-second data transmission using a chip-scale microcomb ring resonator source. *Nat. Photon.* **16**, 798–802 (2022).
46. Rizzo, A. et al. Massively scalable Kerr comb-driven silicon photonic link. *Nat. Photon.* **17**, 781–790 (2023).
47. Shu, H. et al. Microcomb-driven silicon photonic systems. *Nature* **605**, 457–463 (2022).
48. Zhao, Y., Liu, X., Yvind, K., Cai, X. & Pu, M. Widely-tunable, multi-band Raman laser based on dispersion-managed thin-film lithium niobate microring resonators. *Commun. Phys.* **6**, 350 (2023).
49. Schaufele, R. & Weber, M. Raman scattering by lithium niobate. *Phys. Rev.* **152**, 705 (1966).
50. Barker Jr, A. & Loudon, R. Dielectric properties and optical phonons in $LiNbO_3$. *Phys. Rev.* **158**, 433 (1967).
51. Lu, Z. et al. Synthesized soliton crystals. *Nat. commun.* **12**, 3179 (2021).
52. Yang, Q.-F., Yi, X., Yang, K. Y. & Vahala, K. Spatial-mode-interaction-induced dispersive-waves and their active tuning in microresonators. *Optica* **3**, 1132–1135 (2016).
53. Yao, S., Bao, C., Wang, P. & Yang, C. Generation of stable and breathing flat-top solitons via Raman assisted four wave mixing in microresonators. *Phys. Rev. A* **101**, 023833 (2020).
54. Lao, C. et al. Quantum decoherence of dark pulses in optical microresonators. *Nat. Commun.* **14**, 1802 (2023).
55. Yi, X. et al. Single-mode dispersive waves and soliton microcomb dynamics. *Nat. Commun.* **8**, 14869 (2017).
56. Li, J., Diddams, S. & Vahala, K. J. Pump frequency noise coupling into a microcavity by thermo-optic locking. *Opt. Express* **22**, 14559–14567 (2014).
57. Zhang, J. et al. Fundamental charge noise in electro-optic photonic integrated circuits. *Nat. Phys.* **21**, 304–311 (2025).
58. Eid, M. M., Amiri, I. S., Rashed, A. N. Z. & Yupapin, P. Dental lasers applications in visible wavelength operational band. *Indones. J. Electr. Eng. Comput. Sci.* **18**, 890–895 (2020).
59. Bruch, A. W. et al. Pockels soliton microcomb. *Nat. Photon.* **15**, 21–27 (2021).
60. Wang, C. et al. Integrated lithium niobate electro-optic modulators operating at CMOS-compatible voltages. *Nature* **562**, 101–104 (2018).
61. Chen, P.-K. et al. Adapted poling to break the nonlinear efficiency limit in nanophotonic lithium niobate waveguides. *Nat. Nanotechnol.* **19**, 44–50 (2024).
62. Hu, Y. et al. High-efficiency and broadband on-chip electro-optic frequency comb generators. *Nat. Photon.* **16**, 679–685 (2022).
63. Englebert, N. et al. Bloch oscillations of coherently driven dissipative solitons in a synthetic dimension. *Nat. Phys.* **19**, 1014–1021 (2023).
64. Agrawal, G. P. *Nonlinear fiber optics* (Academic Press, 2007).
65. Lugiato, L. A. & Lefever, R. Spatial dissipative structures in passive optical systems. *Phys. Rev. Lett.* **58**, 2209 (1987).
66. Lin, Q., Painter, O. J. & Agrawal, G. P. Nonlinear optical phenomena in silicon waveguides: modeling and applications. *Opt. Express* **15**, 16604–16644 (2007).
67. Kaminow, I. & Johnston Jr, W. Quantitative determination of sources of the electro-optic effect in $LiNbO_3$ and $LiTaO_3$. *Phys. Rev.* **160**, 519 (1967).
68. Bache, M. & Schiek, R. Review of measurements of Kerr nonlinearities in lithium niobate: the role of the delayed Raman response. *Preprint at* https://doi.org/10.48550/arXiv.1211.1721 (2012).
69. Lv, X. et al. Broadband microwave-rate dark pulse microcombs in dissipation-engineered $LiNbO_3$ microresonators. https://doi.org/10.6084/m9.figshare.28282229 (2025).

Acknowledgements

The authors thank Xinrui Luo, Zhenyu Xie, and Zhe Lv for helpful discussions. Q.-F.Y. and X.L. are supported by Beijing Natural Science Foundation (Z210004), National Key R&D Plan of China (Grants No. 2021ZD0301500), and National Natural Science Foundation of China (92150108). C.Y. is supported by National Natural Science Foundation of China (12304412, 12293051). The simulation in this work is supported by the high-performance computing Platform of Peking University. The device fabrication is supported by the Advanced Photonic Integrated Center (APIC) of State Key Laboratory of Advanced Optical Communication System and Networks.

Author contributions

The experiment was conceived by X.L., B.N., and Q.-F.Y. Measurements were performed by X.L. and B.N. with assistance from Z.W. and K.Z. The Raman spectroscopy was performed by B.N. and C.Y. with assistance from G.Z and G.L. The device was fabricated by X.L, C.Y, R.M and Z.C. The device was designed by X.L. with assistance from Y.L. Numerical simulations of comb dynamics were performed by B.N. and D.Q. with assistance from X.J. The project was supervised by Q.G., F.B., and Q.-F.Y. All authors contributed to writing the manuscript.

Competing interests

The authors declare no competing interests.

Additional information

Supplementary information The online version contains supplementary material available at https://doi.org/10.1038/s41467-025-57736-3.

Correspondence and requests for materials should be addressed to Chen Yang, Fang Bo or Qi-Fan Yang.

Peer review information *Nature Communications* thanks the anonymous, reviewers for their contribution to the peer review of this work. A peer review file is available.

Reprints and permissions information is available at http://www.nature.com/reprints

Publisher's note Springer Nature remains neutral with regard to jurisdictional claims in published maps and institutional affiliations.

Open Access This article is licensed under a Creative Commons Attribution-NonCommercial-NoDerivatives 4.0 International License, which permits any non-commercial use, sharing, distribution and reproduction in any medium or format, as long as you give appropriate credit to the original author(s) and the source, provide a link to the Creative Commons licence, and indicate if you modified the licensed material. You do not have permission under this licence to share adapted material derived from this article or parts of it. The images or other third party material in this article are included in the article's Creative Commons licence, unless indicated otherwise in a credit line to the material. If material is not included in the article's Creative Commons licence and your intended use is not permitted by statutory regulation or exceeds the permitted use, you will need to obtain permission directly from the copyright holder. To view a copy of this licence, visit http://creativecommons.org/licenses/by-nc-nd/4.0/.

© The Author(s) 2025